Received: 2 June 2021 | Revised: 30 September 2021 | Accepted: 6 October 2021 | Published on: 8 November 2021

DOI: 10.1002/gamm.202100019

ORIGINAL PAPER

On accurate time integration for temperature evolutions in additive manufacturing

Stefan Kollmannsberger | **Philipp Kopp**

Chair of Computational Modeling and Simulation, Technische Universität München, Munich, Germany

Correspondence
Stefan Kollmannsberger, Chair of Computational Modeling and Simulation, Technische Universität München, Munich, Bavaria, Germany. Email: stefan.kollmannsberger@tum.de

Abstract

We investigate two numerical challenges in thermal finite element simulations of laser powder bed fusion (LPBF) processes. First, we compare the behavior of first- and second-order implicit time-stepping schemes on a fixed domain. While both methods yield comparable accuracies in the pre-asymptotic regime, the second-order method eventually outperforms the first-order method. However, the oscillations present in the pre-asymptotic range of the second-order method can render it less suitable for simulating LPBF processes. Then, we consider sudden domain extensions resulting from subsequently adding new layers of material with ambient temperature. We model this extension on the continuous level in an energy conservative manner. The discontinuities introduced here reduce the convergence order for both time-stepping schemes to 0.75. First and second order accuracy could only be achieved by strongly grading the time-steps towards the domain expansion.

KEYWORDS

additive manufacturing, laser powder bed fusion, temperature evolution, time integration

1 | INTRODUCTION

Laser powder bed fusion (LPBF) is one of many production processes used to additively manufacture artifacts (see e.g., Reference [22] for an overview and classification). Common to all these processes is that raw material is deposited in a layer-wise fashion to create a finished artifact; see, for example, References [2,9] for a current overview of AM processes. The key feature of LPBF is that the raw material is added as powder. Energy is then injected locally by a laser beam. This causes a highly localized and rapid phase change from powder to liquid followed by re-solidification.

The process of LPBF still poses numerous numerical and modeling challenges, including the accurate prediction and control of temperature distributions and residual stresses. Various simulation techniques exist to generate insight. A non-exhaustive list includes the classical finite element method, phase field models and particle methods, see for example, References [12,23] for a detailed collection of possibilities.

1.1 | The problem of scales

The range of scales that appear and need to be resolved in LPBF is very large. Assuming a typical diameter of the laser spot of 100 μm, the simulation of the local solidification needs a resolution of 10 μm or better,

Abbreviations: AM, additive manufacturing; LPBF, laser powder bed fusion.

resulting in 3 to 4 orders of magnitude to reach the size of a (small to moderately large) artifact. A 3D model which uniformly discretizes the structure over the full range of these scales would have to be based on $O(10^9)$ to $O(10^{12})$ cells with an edge-length of 10 μm—which is far beyond the reach of any conventional transient multi-physics simulation. Therefore, it is common to split the scales into three different sections with partial overlaps.

The microscale is responsible for resolving physical phenomena below 1 mm. It delivers insight into the melting/phase-change/solidification process whereby individual grains of powder are resolved. The macroscale resolves physical phenomena from 100 μm up to the part level at a range of 1 cm to 10 cm. It is main purpose is to model the thermal (or thermo-mechanical) behavior at the part level. The mesoscale lies between both and is responsible for the range from 10 μm to 50 μm up to about 1 mm to 10 mm. Since no computational method can capture the full multi-scale and multi-physics nature of the LPBF process in one single computation, a computational model must focus on one scale. Therein it is only possible to include a selected number of physical effects that are specifically relevant for the scale under investigation.

1.2 | The thermal problem an its discretization

In this article, the transient thermal evolution is considered in its simplest form. Nevertheless, such simplified models can provide accurate simulations for the evolution of temperatures of parts [6]. However, even in these simplified models, the challenge of accurately resolving spatial and temporal scales in an accurate yet computationally efficient manner persists. Common ways of bridging spatial and temporal scales are to summarize laser scan lines into equivalent volume loads and apply them at once, to summarize laser scan lines into patches and corresponding equivalent volume loads, and to summarize entire layers in the same manner. This approach leads to a loss of accuracy on the local level, which might prohibit accurate predictions of thermal gradients that are in turn used to predict the evolution of microstructures, for example. To this end, discretization schemes have been proposed which use local refinements in space [7,8,13,18] to resolve these strongly changing gradients in the vicinity of the laser. Such transient discretizations require a careful formulation to deliver accurate results. However, even if the spatial domain is accurately resolved, local oscillations may appear if the time domain is under resolved. Section 2 demonstrates these effects.

Section 3 looks at the possible errors and pitfalls associated with the initialization of new layers. Two techniques known from the simulation of welding processes [15] are commonly utilized to model the layer-wise deposition of material: The *inactive element method* and the *quiet element method*. A comprehensive overview of both strategies is found, for example, in References [4,16], including a discussion of each methods' advantages and disadvantages. In essence, the inactive element method only includes contributions to the global stiffness matrix if material was deposited in the region covered by an element. In the quiet element method, finite elements always contribute but are assigned small conductivities and capacities if no material is present. These two techniques have been available for some time in several commercial products. A third technique is called the finite cell method and relaxes the constraint that each newly added layer must conform to the finite element discretization. Instead, layers may be initialized within elements [3,13]. Section 3.1 presents a corresponding formulation.

Regardless of the technique used, the initialization of newly added layers causes a jump in the initial condition for the first time-step after expanding the domain. As a result, the rates of commonly employed time-stepping schemes deteriorate and do not even reach first-order convergence. This effect is examined in Section 3.2.

Section 3.3 demonstrates that careful attention must be paid to the correct initialization of new layers of material as otherwise energy might be generated artificially at each domain expansion. We demonstrate that introducing artificial energy is avoided by a correct interpretation of the scheme introduced in Section 3.1. The point of view taken in that section is not common practice. Other authors, such as, for example, Reference [17], suggest resetting the temperature at the time-step n to the initial temperature to diminish the artificially introduced energy.

2 | TRANSIENT HEAT EQUATION AND TRANSIENT DISCRETIZATIONS

In this section, we consider a linear thermal model with a fixed domain resembling one laser stroke. The setup is identical to the one introduced in Reference [14], but on top of considering the global convergence in integral norms, we investigate

the local quality of the solution. Given that the range of temporal scales which need to be resolved in time is vast, it is of interest to evaluate the behavior of the time integration for cases in which the time discretization is very coarse. Particularly, we are interested in the local characteristics of the solution for such underresolved scenarios. In the following, we repeat the formulation and convergence study already investigated in Reference [14] in Section 2.1 before we extend the analysis to the local behavior in Section 2.2.2.

2.1 | Formulation

To set the stage for our analysis, we consider the transient heat equation:

$$\begin{aligned} c\frac{\partial T}{\partial t} - \nabla \cdot (k\nabla T) &= Q && \text{on } S \\ T &= T_0 && \text{at } t = 0 \\ T &= T_b && \text{on } \Gamma_D \\ n \cdot k\nabla T &= 0 && \text{on } \Gamma_N, \end{aligned} \tag{1}$$

where S denotes the space-time domain on which the equation is defined and Γ_D and Γ_N are the Dirichlet and Neumann parts of the boundary, such that $\Gamma_D \cap \Gamma_N = \emptyset$. For simplicity but without loss of generality, only pure homogeneous Neumann boundary conditions are considered. Equation (1) is discretized in time using the general-θ scheme. We closely follow Reference [14] in its discretization. The starting point is a first-order differential equation of the following form:

$$\dot{T}(t) = f(t, T) \tag{2}$$

In the general-θ time integration scheme the left hand side is discretized in terms of two time coordinates t^n and t^{n+1} by a finite difference quotient, with a time-step length of $\Delta t = t^{n+1} - t^n$. The right side is interpolated between t^n and t^{n+1} depending on a parameter θ:

$$\frac{\Delta T}{\Delta t} = (1-\theta) f(T^n) + \theta f(T^{n+1}) \tag{3}$$

Different choices result in different time integration schemes:

$$\begin{aligned} \theta = 0 \quad &: \quad \text{Explicit Euler (EE)} \\ \theta = 1/2 \; &: \quad \text{Crank–Nicolson (CN)} \\ \theta = 1 \quad &: \quad \text{Backward Euler (BE)} \end{aligned}$$

We focus on the backward Euler and the Crank–Nicolson methods as the restrictions on the time-step size for $\theta < 0.5$ are impractical for our applications. Now, assuming $c \neq 0 \; \forall \mathbf{x}, t$, the interior part of Equation (1) can be rewritten as follows:

$$\frac{\partial T}{\partial t} = \frac{1}{c}\left[Q + \nabla \cdot (k\nabla T)\right].$$

The general-θ time discretization can then be applied:

$$\frac{\Delta T}{\Delta t} = \frac{(1-\theta)}{c}\left[Q^n + \nabla \cdot (k\nabla T^n)\right] + \frac{\theta}{c}\left[Q^{n+1} + \nabla \cdot (k\nabla T^{n+1})\right],$$

or, with $\Delta T = T^{n+1} - T^n$

$$\frac{c}{\Delta t} T^{n+1} - \theta \nabla \cdot (k\nabla T^{n+1}) = \frac{c}{\Delta t} T^n + \left[(1-\theta)Q^n + \theta Q^{n+1}\right] + (1-\theta)\nabla \cdot (k\nabla T^n). \tag{4}$$

In other words, starting from the initial condition the solution in time is advanced by computing the next solution (at t^{n+1}) using the previous solution (at t^n) as "initial condition." This equation is well defined when Ω does not change (i.e., $S = \Omega \times [0, t^{\max}]$) and can be discretized using a single finite element mesh. To transform Equation (4) into a weak form we take the L^2 inner product with the test functions w:

$$\frac{1}{\Delta t}\langle w, c\ T^{n+1}\rangle - \theta\langle w, \nabla\cdot(k\nabla T^{n+1})\rangle = \frac{1}{\Delta t}\langle w, c\ T^{n}\rangle + \langle w, (1-\theta)Q^n + \theta Q^{n+1}\rangle + (1-\theta)\langle w, \nabla\cdot(k\nabla T^n)\rangle. \tag{5}$$

After integrating by parts we obtain the following weak form: Find $T^{n+1} \in T_b^{n+1} + \mathcal{H}_0^1(\Omega)$, such that

$$\frac{1}{\Delta t}\langle w, c\ T^{n+1}\rangle + \theta\langle \nabla w, k\nabla T^{n+1}\rangle = \frac{1}{\Delta t}\langle w, c\ T^{n}\rangle + \langle w, (1-\theta)Q^n + \theta Q^{n+1}\rangle - (1-\theta)\langle \nabla w, k\nabla T^n\rangle \tag{6}$$

holds for all $w \in \mathcal{H}_0^1(\Omega)$. Choosing a discrete subspace $\mathcal{W}^h(\Omega) \subset \mathcal{H}^1(\Omega)$ spanned by the basis functions $N_i(x)$ yields the following matrix equation:

$$\underbrace{\left[\frac{1}{\Delta t}\mathbf{C} + \theta\mathbf{K}\right]}_{\mathbf{A}}\hat{\boldsymbol{T}}^{n+1} = \underbrace{\left[\frac{1}{\Delta t}\mathbf{C} - (1-\theta)\mathbf{K}\right]\hat{\boldsymbol{T}}^{n} + (1-\theta)\boldsymbol{Q}^n + \theta\boldsymbol{Q}^{n+1}}_{\mathbf{F}}, \tag{7}$$

or in short $\mathbf{A}\hat{\boldsymbol{T}}^{n+1} = \mathbf{F}$. Therein, $\hat{\boldsymbol{T}}^{n+1}$ are the coefficients for to the discretization of time t^{n+1} and

$$\begin{aligned} A_{ij} &= \int_\Omega \frac{c}{\Delta t} N_i N_j + \kappa\ \theta\ \nabla N_i \cdot \nabla N_j \,\mathrm{d}\Omega \\ F_i &= \int_\Omega N_i \left(\frac{c}{\Delta t} T^n + \theta Q^{n+1} + (1-\theta)Q^n\right) - \kappa\ (1-\theta)\ \nabla N_i \cdot \nabla T^n \,\mathrm{d}\Omega. \end{aligned} \tag{8}$$

This way of writing Equation (8) is chosen to emphasize the following crucial point: The basis functions N_i and N_j in Equation (8) belong to the discretization of time t^{n+1}. However, the old solution T^n and its derivatives ∇T^n belong to the discretization of time t^n. The consequence of this is that an implementation must provide two bases (for t^n and for t^{n+1}) to assemble the equation system of time-step $n+1$. Moreover, an accurate Gaussian integration of these mixed integrals requires sufficient continuity. In our implementation this is ensured by applying a partitioned integration on the intersection of the meshes used to discretize the time-steps t^n and t^{n+1}.

2.2 | Example

We now solve Equation (7) using the recently introduced extension to the multi-level *hp* framework described in Reference [14] using a similar example as described therein. We demonstrate that the formulation given in Equation (8) provides the expected convergence rate in time for dynamic spatial refinements. To this end, we investigate the heat source $q(x, y, z)$ traveling along the path $p = \mathbf{x}(t)$. Together with intensity $I(t)$ that determines the power over time we define the source function $Q(x, y, z, t)$ as

$$Q(\boldsymbol{x}, t) = I(t)\ q\left(x - p_x(t), y - p_y(t), z - p_z(t)\right),$$

with q defined as a Gaussian function centered at the origin:

$$q(x, y, z) = \frac{1}{(2\pi)^{3/2}\ \sigma^3}\ \exp\left(\frac{-x^2 - y^2 - z^2}{2\sigma^2}\right). \tag{9}$$

This type of heat source was first introduced for welding by Goldak [11] but is also commonly used in LPBF processes, see for example, Reference [1]. Assuming a steady-state with constant temperature T_0 at $t = 0$, we define the semi-analytical solution on an infinite domain as follows

$$
\begin{aligned}
{}^{ex}T(x,y,z,t) &= \int_0^t I(\tau)\; g\left(x - p_x(\tau), y - p_y(\tau), z - p_z(\tau),\; t - \tau\right)\; \mathrm{d}\tau + T_0 \\
g(x,y,z,t) &= \frac{1}{c\;(2\pi)^{3/2}\;w(t)^3}\;\exp\left(\frac{-x^2 - y^2 - z^2}{2w(t)^2}\right) \\
w(t) &= \sqrt{\sigma^2 + \frac{2\kappa t}{c}}.
\end{aligned}
\tag{10}
$$

In Equation (10), g is the result of analytically computing the convolution integral of q with the fundamental solution of the heat equation (i.e., Equation (1) with $Q = \delta(x,y,z,t)$). The solution is then obtained from a second convolution integral in time that adds up all previous positions (according to p) with the respective intensity I. This second convolution integral is computed numerically using a partitioned Gauss–Legendre rule in time that we chose accurate enough for our convergence studies. For a generic formulation depending on the dimensionality, see Reference [14]. Figure 1 shows the geometric setup and the model parameters. Furthermore, we choose a zero flux condition on the top side and fix the temperatures on the other sides according to Equation (10).

Figure 2 shows the solution at t_{max} after 256 Crank–Nicolson steps. The meshes for each time-step are refined locally towards the current position of $p(t)$. We set the polynomial degrees depending on the refinement depth to 5, 6, 6, 5, 4 and 3, for levels 0 to 5, respectively.

2.2.1 | Convergence

To verify our implementation, we perform convergence studies for the Crank–Nicolson and the backward Euler versions. The errors are measured by computing the L^2 norm on each time slice and integrating them in time using a trapezoidal rule. The results are shown in Figure 3. The second-order accurate Crank–Nicolson scheme exhibits a pre-asymptotic

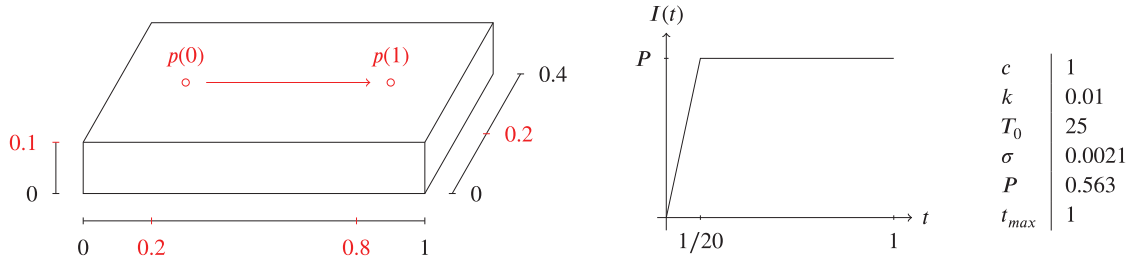

FIGURE 1 Domain and path definitions, intensity function and problem parameters. Reprinted from Reference [14]

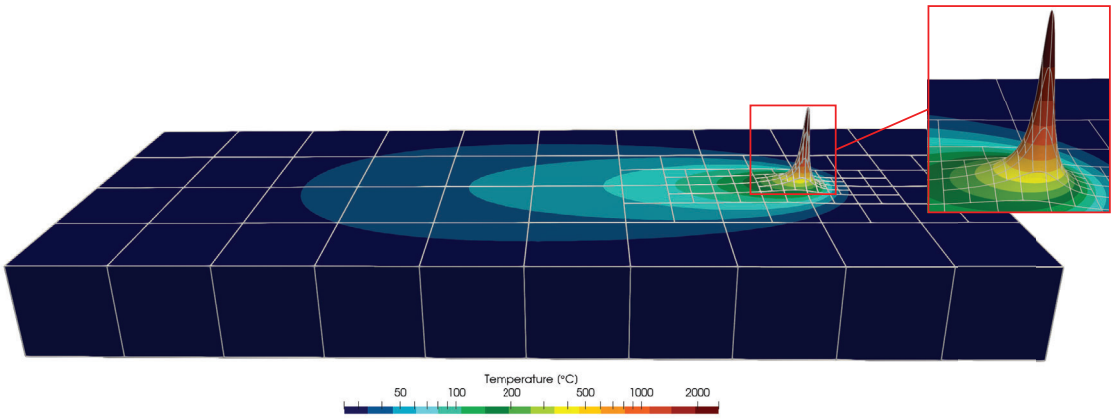

FIGURE 2 Solution at $t = 1$ using a logarithmic color map

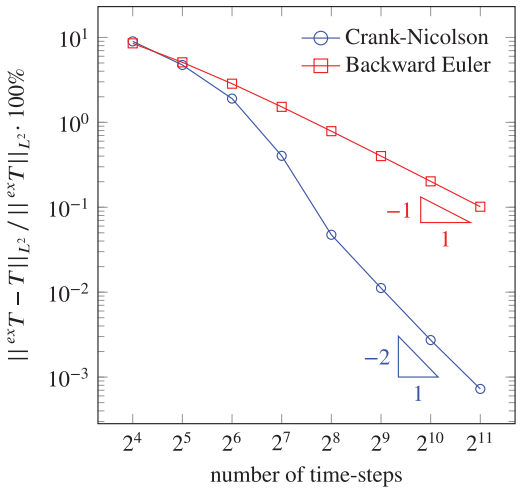

FIGURE 3 Convergence of the temporal refinement. Reprinted from Reference [14]

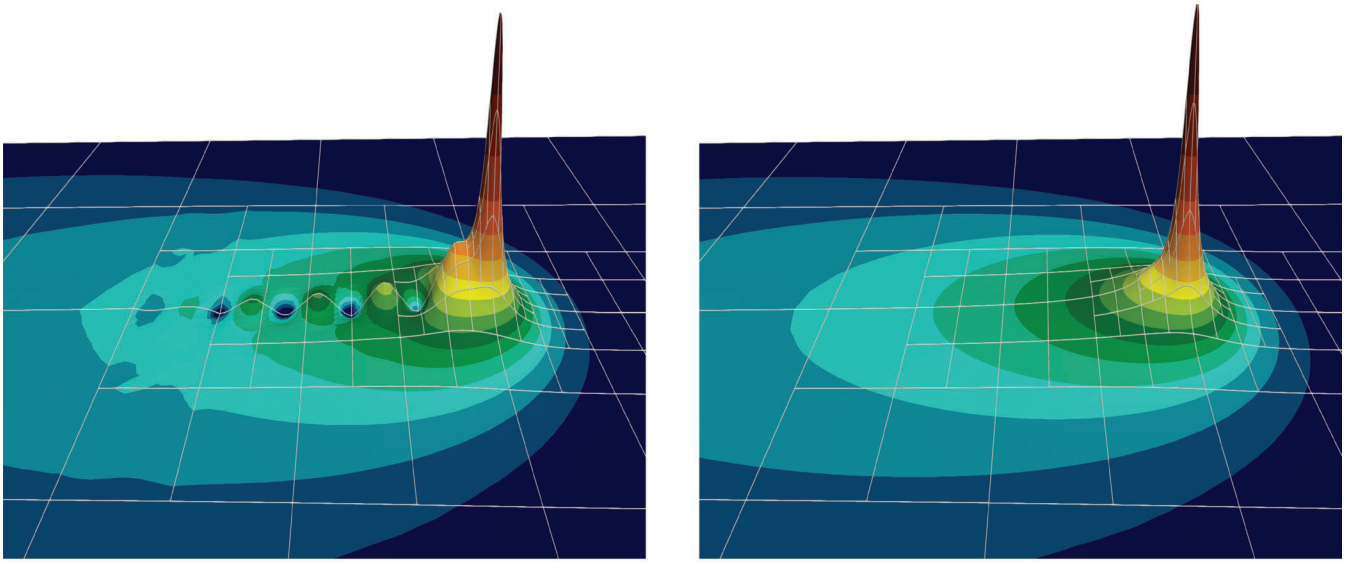

(A) Crank-Nicolson (B) Backward Euler

FIGURE 4 Solution at $t = 1$ using 32 time-steps

regime ranging from 16 to about 256 time-steps. In the asymptotic regime, both schemes show the expected first- and second-order rates of convergence.

2.2.2 | Local quality

Given these results and the vast range of scales, one might be tempted to choose the Crank–Nicolson scheme and use as few time-steps as possible. This results in as little effort as possible but commonly enters the pre-asymptotic regime. In addition to assessing the quality of the method using global integral norms, we now discuss the local characteristics of the solution for simulating LPBF processes. Time-marching schemes of higher orders (more than first-order) are known to exhibit oscillations. These are very prominent in a temporally underresolved setting, that is, in the pre-asymptotic range, as shown in Figure 4. While 32 time-steps are too few to expect reliable results, the oscillations in the wake of the laser are also clearly observable approximately until the asymptotic convergence has been reached. In contrast, the backward Euler method produces physically meaningful results even for very underresolved cases.

As a result, the backward Euler scheme is much more popular for under-resolved time integration. We want to stress that the difference is in the *shape* of the error rather than the *amount*. While the oscillations in the second-order method are clearly noticeable, the over-diffusive nature of the backward Euler scheme renders its errors much more subtle. Similar arguments have been made concerning the *p*-version of the finite element method for decades. Although *hp* methods that tackle these issues are well established and exist for a long time, high-order methods are still often not highly appreciated in practical applications.

Strongly changing temperature gradients also occur if the domain suddenly expands because a new layer is deposited. This problem is quite similar to the one discussed in this section and will be addressed next.

3 | TRANSIENT HEAT EQUATION ON EXPANDING DOMAINS

In this section, we introduce a model to treat expanding domains. This is inherent to the process of depositing new layers of material upon the already existing substrate. The model contains two numerical challenges. First, the newly added layer must be correctly initialized to not introduce energy into the system. Unlike existing methods, our approach performs these domain extensions in the continuous setting and therefore does not depend on the discretization. Second, a suddenly added cold metal powder introduces a discontinuity in space and time that must be treated appropriately. We use a locally refined finite element mesh in combination with strongly graded time-steps to recover the expected convergence rates.

3.1 | Formulation

We consider a domain Ω which is extended in a stepwise fashion throughout the simulation. Assuming that the extensions happen at t^k, we obtain a series of domains Ω_k corresponding to each interval $[t^k, t^{k+1}]$. Associated with each extension is also an increment $\Delta\Omega_k = \Omega_{k+1} \setminus \Omega_k$. Figure 5 depicts a single extension for a transient one-dimensional problem. When defining our heat problem for this setup we must provide an initial condition for each $\Delta\Omega_k$ to ensure well-posedness in the continuous setting. While the choice is generally arbitrary, it makes sense to assume that the temperature of newly added layer is equal to the ambient temperature T^∞. Hence, our initial condition for advancing the solution from t_k to t_{k+1} is defined as follows:

$$T_{\Omega_{k+1}}(\boldsymbol{x}, t) = T_e(\boldsymbol{x}, t) = \begin{cases} T_{\Omega_k}(\boldsymbol{x}, t) & \text{if} \quad \boldsymbol{x} \in \Omega_k \\ T^\infty & \text{if} \quad \boldsymbol{x} \in \Delta\Omega_k \end{cases} \tag{11}$$

in which T_e denotes the extended temperature field. After consistently formulating the continuous problem, we discretize each slab $S_k = \Delta\Omega_k \times [t^k, t^{k+1}]$ using the methodology discussed in Section 2. By adding the time-steps of all slabs, we obtain a partitioned time-stepping scheme. At several points in time the domain is extended from one time-step to another. Assume, that one of these extensions happens at t^n (between time-steps n and $n+1$), where n now represents the time-step index while k represents the domain index. This involves the following steps:

1. Compute T^n from T^{n-1} on Ω_k
2. Extend the domain by $\Delta\Omega_k$; T^n now changes to T_e^n as given by Equation (11)
3. Compute T^{n+1} using T_e^n on Ω_{k+1}

Step 2 is more of theoretical nature and sets the stage for a consistent continuation of the time-stepping scheme. The question is now how to handle the piecewise-defined initial condition in Step 3. Inserting T_e^n into the weak form given by Equation (5) yields

$$\frac{1}{\Delta t}\langle w, c\ T^{n+1}\rangle - \theta\langle w, \nabla\cdot(k\nabla T^{n+1})\rangle = \frac{1}{\Delta t}\langle w, c\ T_e^n\rangle + \langle w, (1-\theta)Q^n + \theta Q^{n+1}\rangle + (1-\theta)\langle w, \nabla\cdot(k\nabla T_e^n)\rangle \tag{12}$$

In the general case, T_e^n possesses a discontinuity at the interface between Ω_k and $\Delta\Omega_k$ (see Equation (11)). Most literature suggests that the general-θ scheme is unconditionally stable and reaches second-order convergence for $\theta = 0.5$. However, the order of convergence achieved may be less for non-smooth initial data. This is nicely pointed out in Reference [10]. Additionally, Equation (12) also contains the spatial derivatives of the discontinuous function T_e^n. Rannacher analyzed the instability caused by discontinuous initial conditions in Reference [21] in the context of the computation

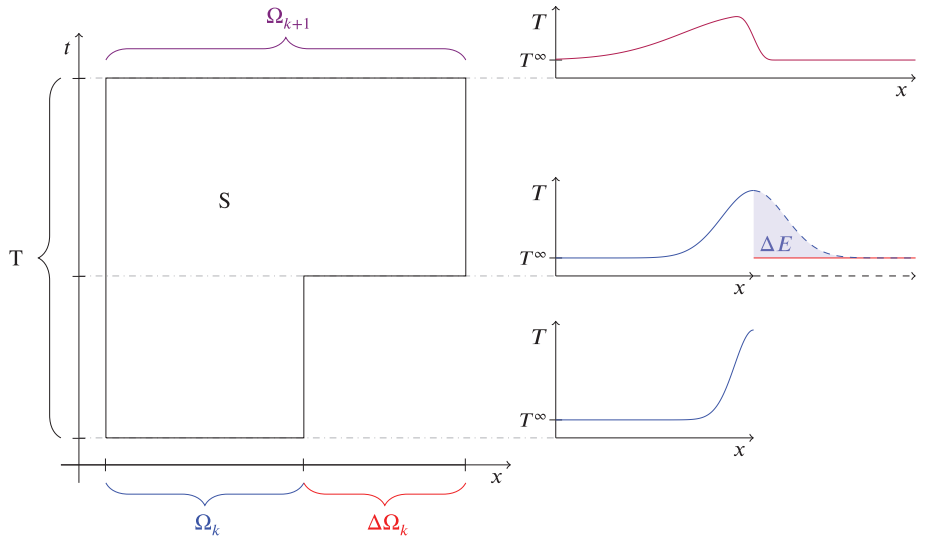

FIGURE 5 Domain extension in space-time

of values of stock options to smooth out discontinuous initial data. As a remedy, the authors of Reference [21] propose to replace the first two time-steps after imposing the discontinuous initial data with two backward Euler time-steps with $\frac{\Delta t}{2}$ right after this discontinuity is introduced. The purpose of the backward Euler steps is to introduce high-frequency damping numerically, which smooths out the pollution error present after the shock is experienced. Also, with $\theta = 1$ the diffusion term at the right-hand side of Equation (12) vanishes. We then split the integration of $\langle w, c\ T_e^n \rangle$, which is now defined on Ω_{k+1} such that:

$$\langle w, c\ T_e^n \rangle_{\Omega_{k+1}} = \langle w, c\ T^n \rangle_{\Omega_k} + \langle w, c\ T^\infty \rangle_{\Delta\Omega_k}$$

After integrating by parts, we obtain the following modified weak form for $\theta = 1$:

$$\frac{1}{\Delta t}\langle w, c\ T^{n+1} \rangle_{\Omega_{k+1}} + \langle \nabla w, k \nabla T^{n+1} \rangle_{\Omega_{k+1}} = \frac{1}{\Delta t}\langle w, c\ T^n \rangle_{\Omega_k} + \frac{1}{\Delta t}\langle w, c\ T^\infty \rangle_{\Delta\Omega_k} + \langle w, Q^{n+1} \rangle_{\Omega_{k+1}} \tag{13}$$

for the time-step(s) right after the expansion. The discrete counterpart simply reads:

$$\underbrace{\left[\frac{1}{\Delta t}\mathbf{C}_{\Omega_{k+1}} + \mathbf{K}_{\Omega_{k+1}}\right]}_{\mathbf{A}}\hat{\boldsymbol{T}}^{n+1} = \underbrace{\frac{1}{\Delta t}\mathbf{C}_{\Omega_k}\hat{\boldsymbol{T}}^n + \frac{1}{\Delta t}\hat{\boldsymbol{T}}_\infty^{n+1} + \boldsymbol{Q}^{n+1}}_{\mathbf{F}} \tag{14}$$

where

$$\hat{\boldsymbol{T}}_\infty^{n+1} = \int_{\Delta\Omega_k} N_i\ c\ T^\infty\ \mathrm{d}\Omega.$$

Note that $\mathbf{C}_{\Omega_k}$ is a rectangular matrix as it uses test functions defined on Ω_{k+1} and trial functions defined on Ω_k. It lifts the size of $\hat{\boldsymbol{T}}^n$ to the size of $\hat{\boldsymbol{T}}^{n+1}$. Preferably, an implementation would directly assemble the result of this matrix-vector product. Additionally, the same result can be obtained by first computing the L^2 projection $T_e^{n,h} = N_i \hat{T}_{e,i}^n$ of T_e^n onto the finite element space defined on Ω_{k+1}, and then simply continuing with the usual time-stepping using $\mathbf{C}_{\Omega_{k+1}}\hat{\boldsymbol{T}}_e^n$. This follows from the fact that the L^2 projection satisfies

$$\langle N_i, T_e^{n,h} \rangle_{\Omega_{k+1}} = \langle N_i, N_j \rangle_{\Omega_{k+1}} \hat{T}_{e,j}^n = \langle N_i, T_e^n \rangle_{\Omega_{k+1}}$$

for all N_i by definition and hence can be used instead.

In the ghost finite element method (or the finite cell method) in additive manufacturing, the domain extension is modeled by successively activating elements that form $\Delta\Omega_k$. In this context, deactivating means eliminating the influence

of the residual by multiplying it with an indicator function

$$\alpha^k(\boldsymbol{x}) = \begin{cases} 1 & \text{if } \boldsymbol{x} \in \Omega_k \\ \epsilon & \text{else} \end{cases},$$

where ϵ is a small value $\ll 1$ to preserve definiteness. For $\epsilon \to 0$, the original solution is recovered. Moreover, an indicator function for $\Delta\Omega_k$ is obtained by subtracting α^k from α^{k+1}. Together, these modifications allow using the same (base-) mesh throughout the entire simulation. As a result, the dimensions of all matrices and vectors do not change between time-steps by defining Equation (15) on a single domain Ω using different α's:

$$\frac{1}{\Delta t}\langle w, \alpha^{k+1} c\ T^{n+1} \rangle_{\Omega_{k+1}} + \langle \nabla w, \alpha^{k+1} k \nabla T^{n+1} \rangle_{\Omega} = \frac{1}{\Delta t}\langle w, \alpha^k c\ T^n \rangle_{\Omega} + \frac{1}{\Delta t}\langle w, \left(\alpha^{k+1} - \alpha^k\right)\ c\ T^{\infty} \rangle_{\Omega} + \langle w, Q^{n+1} \rangle_{\Omega} \tag{15}$$

Restating the problem such that $T^{\infty} = 0$ might be beneficial to simplify the model. To not introduce artificial energy into the system, the first time-step after a domain extension must use $\mathbf{C}^n$, where

$$C_{ij}^n = \langle N_i, \alpha^k c\ N_j \rangle_{\Omega}$$

is the mass matrix integrated with respect to the part of Ω that was active before the extension. This way, contributions from basis functions with support in $\Delta\Omega_k$ are masked correctly. Using $\mathbf{C}^{n+1}$ instead of $\mathbf{C}^n$ requires either an L^2 projection similar to the one suggested above or alternatively subtracting the additional energy by a correction term on the right-hand side that acts as a heat sink.

3.2 | Convergence

To analyze the convergence behavior we consider the scenario shown in Figure 5 with $\Omega_0 = [0, 1/2]$ and $\Omega_1 = [0, 1]$. We choose a constant initial temperature $T_0 = 1$ and the ambient temperature $T^{\infty} = 0$. As the initial condition is constant and nothing happens before the domain extension, we reduce the problem to an equivalent formulation with discontinuous initial data instead of a domain extension. Hence, T^0 becomes the following step function

$$T_0(x) = \begin{cases} 1 & \text{if } x \leq 1/2 \\ 0 & \text{else} \end{cases}. \tag{16}$$

Analytical solutions for discontinuous initial conditions are well-known in the literature. For our setting, we obtain

$${}^{ex}T_{\Omega_k}(x, t) = \frac{1}{2} + \frac{1}{2}\text{erf}\left(\frac{0.5 - x}{\sqrt{4t}}\right) \qquad t > 0, \tag{17}$$

where erf$(\cdot)$ is the Gauss error function. To compare different time-stepping schemes, we choose a very short time domain of $[0, t_{max}]$ with $t_{max} = 10^{-3}$. Figure 6A sketches the analytical solution for selected time-steps. Starting from the step function T_0, the solution diffuses out over time.

We first discretize the domain with 512 finite elements of equal length with degree $p = 1$ and compare the solution for the backward Euler and Crank–Nicolson methods for 32 equally spaced time-steps in Figure 6B,C. The initial set of unknowns for all time-stepping schemes is obtained from an L^2 projection of Equation (16) onto the finite element space. The solution is shown after the first time-step at $t_1 = t_{max}/32$, for $t_{max}/2$, and for t_{max}, along with the analytical solution at t_{max}. As expected, the Crank–Nicolson scheme yields clearly noticeable oscillations within the observed time. Choosing smaller time-steps does not reduce the oscillations within the initial time-steps, but does improve the overall solution afterwards. In contrast, the backward-Euler scheme does not produce any visible artifacts regardless of the time-step size. We then construct a hybrid approach following [21] where we use a Crank–Nicolson scheme with N time-steps and subdivide the first time-step into another N backward Euler steps. Such an approach was also proposed in References [19,20]. Figure 6D shows that this approach can combine the benefits of both approaches successfully.

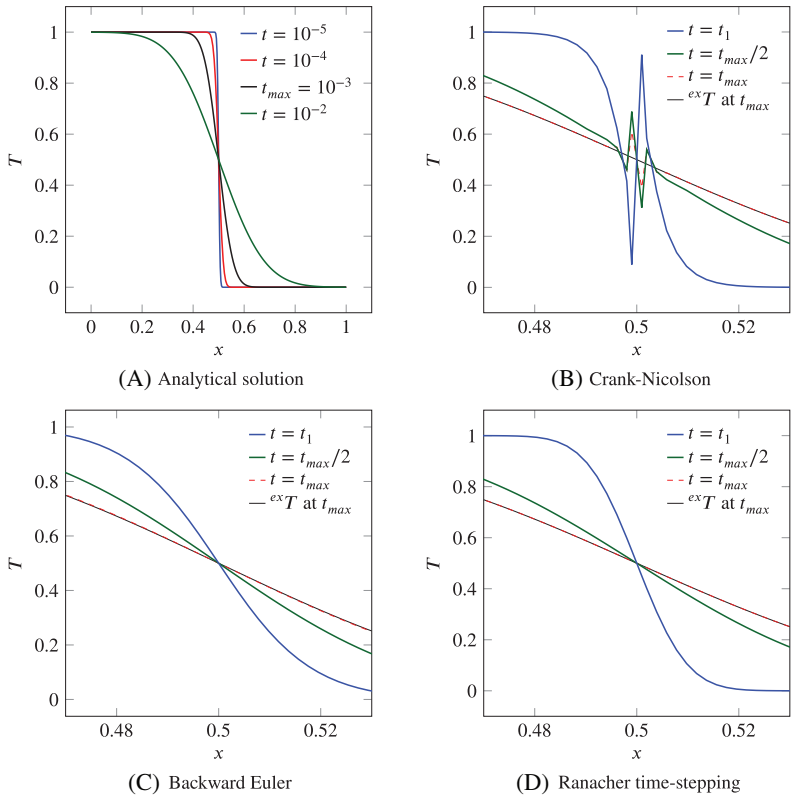

(A) Analytical solution (B) Crank-Nicolson

(C) Backward Euler (D) Ranacher time-stepping

FIGURE 6 Solutions using different time-integration schemes

To investigate the convergence in time, we use an *hp* refined finite element mesh in space with 8 base elements, 8 levels of refinement towards the discontinuity, and polynomial degree 12. This ensures that the error from the spatial discretization does not dominate the error from the time discretization. The convergence of all schemes is compared in Figure 7. The Crank–Nicolson scheme performs very poorly on this example, both, regarding its accuracy and rate of convergence. The backward Euler method performs slightly better but does also not reach the expected rate. While the Rannacher method performs reasonably well initially, it deteriorates afterwards to the same rate as the backward Euler method. This is not surprising considering that the initial steps are backward Euler and eventually dominate the convergence.

This dismal performance can clearly be attributed to the discontinuous initial condition. To recover the expected rates of convergence promised by the backward Euler and the Crank–Nicolson methods, we geometrically grade the time-steps towards the discontinuous initial condition. Introducing a grading factor g that determines the strength of the grading, we subdivide the time interval $[0, t_{max}]$ in a non-uniform fashion:

$$t_i = \frac{10^{gi/N} - 1}{10^g - 1}\, t_{max}, \tag{18}$$

where N is the number of time-steps. Moreover, we compute the time-step length as

$$\Delta t_i = t_{i+1} - t_i = 10^{gi/N} \frac{10^{g/N} - 1}{10^g - 1}\, t_{max}. \tag{19}$$

As shown in Figures 7 and 8, this approach recovers second-order convergence for $g \geq 6$ for the Crank–Nicolson scheme and first-order convergence for the backward Euler scheme for $g \geq 2$. The grading is quite strong as, for example, for $g = 6$ already 95% of the time-steps lie in the first half of the time interval. While such strong gradings may not be practical, the ultimate goal is to develop a methodology for simulating sudden domain extensions in a consistent and numerically "friendly" manner. To this end, we must ensure that these discontinuities are resolved without artificial oscillations and

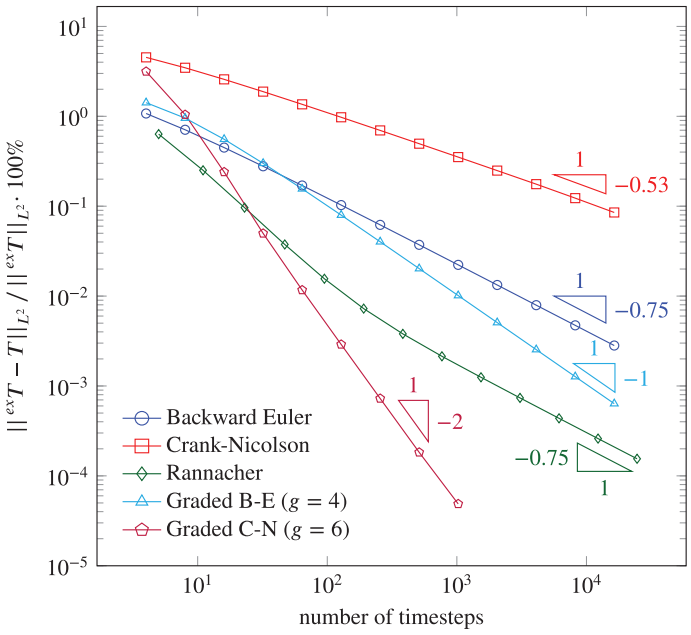

FIGURE 7 Convergence different time integration schemes

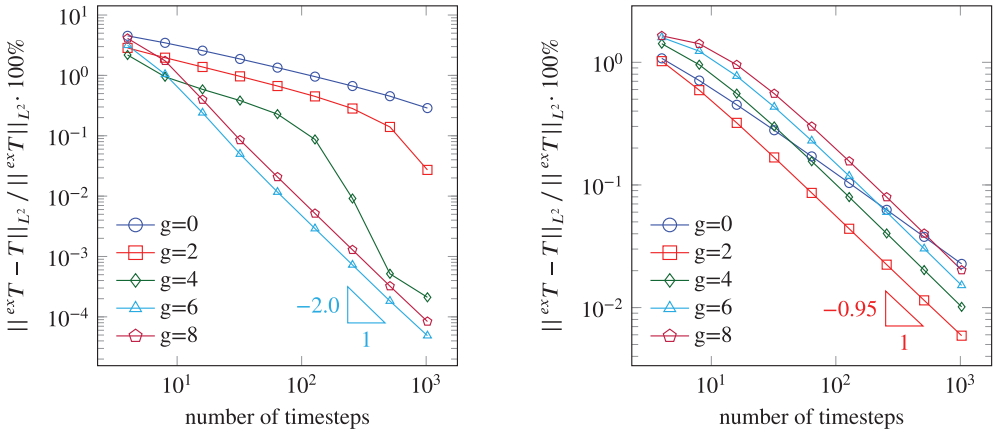

(A) Crank-Nicolson method

(B) Backward Euler method

FIGURE 8 Comparison of different grading factors as given by Equation (18)

with sufficient accuracy to not dominate the overall simulation error. A promising approach seems to be the Rannacher method proposed in Reference [21] as this combines the best out of the two schemes we considered here.

3.3 | A 3D example

To demonstrate the framework introduced in Section 3.1, we now consider a three-dimensional example with multiple domain extensions. Other approaches such as the one used in Reference [17] lead to an introduction of artificial energy. To show that our method is conservative, we consider the example depicted in Figure 9. It consists of a base plate with the dimensions 47.625 mm × 15.0 mm × 5.6896 mm. A built structure emerges as a wall centered on the top face with dimensions 38.1 mm × 3 mm upon which 60 layers are placed subsequently starting from the base plate, each with a thickness of 0.2032 mm. The material properties are chosen as $\kappa = 17.5 \times 10^{-3}$ W/(mmK), $\rho = 4.43{\times}10^{-6}$ kg/mm^3, $c = 1 \times 10^3$ J/(kg K), similar to a Titanium alloy. However, for

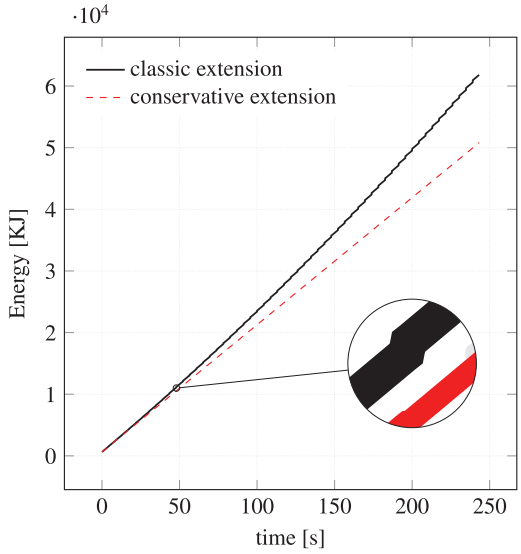

(A) Comparison of energies

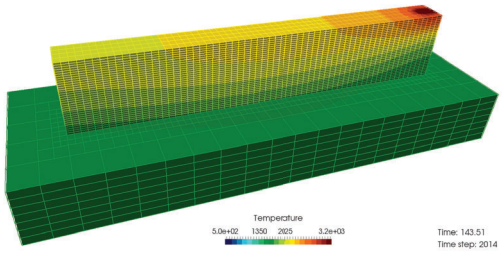

(B) classic extension

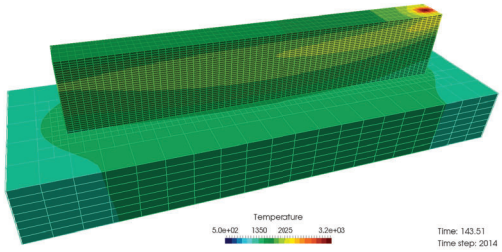

(C) Energy conservative extension

FIGURE 9 Energy conservative and classic extension schemes

simplicity, the material behavior is assumed to be linear, that is, the coefficients do not depend on the temperature. The heat source has a velocity of $v = 8.466\,\text{mm/s}$ and is modeled by a variant of Equation (9) as given in Equation (20)

$$q(x,y,z) = \frac{6\sqrt{3}Pv}{\sigma_1\sigma_2\sigma_3\pi\sqrt{\pi}} \exp\left(-3\left(\frac{x^2}{\sigma_1^2} + \frac{y^2}{\sigma_2^2} + \frac{z^2}{\sigma_3^2}\right)\right). \tag{20}$$

The geometry of the source is determined by $\sigma_1 = 1.5$ $\sigma_2 = 0.9$, and $\sigma_2 = 1.5$. The laser power is assumed as $P = 425\,\text{W}$ and the process efficiency to $v = 0.45$. After each deposition of a layer, there is one time-step in which no heat source is applied to mimic the latency in a coating process. From the second time-step on, the heat source travels along one single stroke for 35.72 mm at the center line of the recently deposited layer. We discretize the laser path by 60 time-steps, each with a length of $\Delta t = 70.32\,\text{ms}$. This corresponds to approximately two time-steps per diameter of the heat source, which is considered sufficient in these types of under-resolved simulations. In order not to suffer from instabilities, a backward Euler scheme is chosen.

This treatment of the heat source and neglecting any nonlinearities is an over-simplification of the process and can, therefore, not be used to predict the local evolution of micro-structures. Nevertheless, these linearized models deliver sufficiently accurate results if the region of interest is far enough away from the melt pool [5]. This is the case, for example, if local hot spots are to be identified within the artifact.

We then integrate the total energy contained in the artifact over all time-steps and depict the obtained values in Figure 9A. The red line represents a conservative extension that increases linearly with time. The black line, called classic extension, delivers higher total energy. The difference can be attributed to the inconsistent initialization of the temperature in each layer. Figure 9B,C show that these differences result in noticeably different temperature distributions.

4 | CONCLUSIONS

Given the vast temporal scales involved in the process of LPBF, higher-order convergence rates in time are of interest in the discretization of LPBF processes. Transient simulations in LPBF processes often employ the first-order backward Euler method or the second-order Crank–Nicolson method. Even though such higher-order methods perform

better asymptotically, unphysical local oscillations can appear in the solution in the pre-asymptotic range. This may severely limit the applicability of such methods for simulating LPBF processes, given the large time scales that need to be resolved.

Similar problems appear when consistently modeling expanding domains. These sudden expansions result in discontinuous initial conditions in the time-stepping schemes. We demonstrate that this reduces the convergence rates to 0.5 for the Crank–Nicolson method and 0.75 for the backward Euler method. An alternative is to use the Rannacher time-stepping scheme, which delivers a better constant but shows only a convergence rate of 0.75 in the investigated example. The expected order of accuracy of the Crank–Nicolson scheme could only be achieved using a strong grading of the time-steps towards the discontinuous initial condition.

In practical applications strongly changing gradients are avoided in time either by using time-averaged heat inputs or by introducing a sufficiently long dwelling time step. These approximations can still lead to sufficiently accurate yet computationally efficient predictions for practical applications. For example: The temperature evolution during the dwelling time has only little effect on the size of the melt pool and may, therefore, be computed with poor accuracy if the quantity of interest is the size of the melt pool. Another example is the fact that for an estimation of the global temperature evolution, a time-averaged heat input leads to sufficiently accurate results. However, if the full scale of temporal and spatial scales needs to be captured, then an accurate resolution of rapidly changing gradients must be addressed on all scales present in the heat evolution of a LPBF process in space and time. Such a scale-integrative analysis is currently beyond the reach of available discretization methods partially because they face the difficulties highlighted in this contribution.

Promising alternatives to the investigated classic finite-difference-based time-stepping procedures are adaptive space-time methods. These are not discussed here but would allow for a localization of the discretization towards strongly changing gradients. Therefore, they can deliver higher convergence rates in time for the numerical challenges discussed in this contribution.

ACKNOWLEDGEMENT

We gratefully acknowledge the support of the German Research Foundation under Grant No. KO 4570/2-1. Open Access funding enabled and organized by Projekt DEAL.

REFERENCES

[1] M. I. Al Hamahmy and I. Deiab, Review and analysis of heat source models for additive manufacturing, Int. J. Adv. Manuf. Technol. **106** (2020), no. 3–4, 1223–1238.

[2] K. Babak and Wohlers Report, *3D printing and additive manufacturing global state of the industry*, Wohlers Associates, Inc., 2021. https://wohlersassociates.com/2021report.htm

[3] M. Carraturo, J. Jomo, S. Kollmannsberger, A. Reali, F. Auricchio, and E. Rank, Modeling and experimental validation of an immersed thermo-mechanical part-scale analysis for laser powder bed fusion processes, Addit. Manuf. **36** (2020), 101498.

[4] M. Chiumenti, M. Cervera, A. Salmi, C. Agelet de Saracibar, N. Dialami, and K. Matsui, Finite element modeling of multi-pass welding and shaped metal deposition processes, Comput. Methods Appl. Mech. Eng. **199** (2010), no. 37–40, 2343–2359.

[5] M. Chiumenti, E. Neiva, E. Salsi, M. Cervera, S. Badia, J. Moya, Z. Chen, C. Lee, and C. Davies, Numerical modelling and experimental validation in selective laser melting, Addit. Manuf. **18** (2017), 171–185.

[6] M. Chiumenti, X. Lin, M. Cervera, W. Lei, Y. Zheng, and W. Huang, Numerical simulation and experimental calibration of additive manufacturing by blown powder technology. Part I: Thermal analysis, Rapid Prototyp. J. **23** (2017), no. 2, 448–463.

[7] D. D'Angella, S. Kollmannsberger, E. Rank, and A. Reali, Multi-level Bézier extraction for hierarchical local refinement of isogeometric analysis, Comput. Methods Appl. Mech. Eng. **328** (2018), 147–174.

[8] E. Denlinger, "*Chapter 12 - development and numerical verification of a dynamic adaptive mesh coarsening strategy for simulating laser power bed fusion processes*," *Thermo-mechanical modeling of additive manufacturing*, M. Gouge and P. Michaleris (eds.), Butterworth-Heinemann, Oxford, UK, 2018, pp. 199–213.

[9] I. Gibson, D. W. Rosen, B. Stucker, and M. Khorasani, *Additive manufacturing technologies*, Springer Nature, Switzerland AG, 2021.

[10] M. B. Giles and R. Carter, *Convergence analysis of crank-Nicolson and Rannacher time-marching*, Vol **9**, Oxford University Computing Laboratory, Oxford, UK, 2005, 89–112.

[11] J. Goldak, A. Chakravarti, and M. Bibby, A new finite element model for welding heat sources, Metall. Trans. B **15** (1984), no. 2, 299–305.

[12] M. Gouge, P. Michaleris, E. Denlinger, and J. Irwin, "*The finite element method for the Thermo-mechanical modeling of additive manufacturing processes, Thermo-mechanical modeling of additive manufacturing*," M. Gouge, P. Michaleris, *Thermo-mechanical modeling of additive manufacturing*, Butterworth-Heinemann, Elsevier, Oxford, UK, 2018, pp. 19–38. https://doi.org/10.1016/B978-0-12-811820-7.00003-3

[13] S. Kollmannsberger, A. Özcan, M. Carraturo, N. Zander, and E. Rank, A hierarchical computational model for moving thermal loads and phase changes with applications to selective laser melting, Comput. Math. Appl. **75** (2018), no. 5, 1483–1497.

[14] P. Kopp E. Rank, V. M. Calo, and S. Kollmannsberger, *Efficient multi-level hp-finite elements in arbitrary dimensions*, 2021. arXiv:2106.08214 [cs, math].
[15] L. Lindgren, *Computational welding mechanics thermomechanical and microstructural simulations*, Woodhead Publishing, Abington, Cambridge, UK, 2007.
[16] L.-E. Lindgren and E. Hedblom, Modelling of addition of filler material in large deformation analysis of multipass welding, Commun. Numer. Methods Eng. **17** (2001), no. 9, 647–657.
[17] P. Michaleris, Modeling metal deposition in heat transfer analyses of additive manufacturing processes, Finite Elem. Anal. Des. **86** (2014), 51–60.
[18] E. Neiva, S. Badia, A. F. Martín, and M. Chiumenti, A scalable parallel finite element framework for growing geometries. application to metal additive manufacturing, Int. J. Numer. Methods Eng. **119** (2019), 1098–1125.
[19] O. Østerby, Five ways of reducing the crank–Nicolson oscillations, BIT Numer. Math. **43** (2003), no. 4, 811–822.
[20] C. E. Pearson, Impulsive end condition for diffusion equation, Math. Comput. **19** (1965), no. 92, 570–576.
[21] R. Rannacher, Finite element solution of diffusion problems with irregular data, Numer. Math. **43** (1984), no. 2, 309–327.
[22] C. B. Williams, F. Mistree, and D. W. Rosen, A functional classification framework for the conceptual design of additive manufacturing technologies, J. Mech. Des. **133** (2011), no. 12, 121002.
[23] T. I. Zohdi, *Modeling and simulation of functionalized materials for additive manufacturing and 3D printing: Continuous and discrete media*, Lecture Notes in Applied and Computational Mechanics, Vol **60**, Springer International Publishing, Cham, Switzerland, 2018. https://doi.org/10.1007/978-3-319-70079-3

How to cite this article: S. Kollmannsberger, and P. Kopp, *On accurate time integration for temperature evolutions in additive manufacturing*, GAMM-Mitteilungen. **44** (2021), e202100019. https://doi.org/10.1002/gamm.202100019